Implementation of a modified Graham-Walles viscosity function within a Chaboche viscoplastic constitutive model

Carlos Rojas-Ulloa*[a], Hélène Morch[a], Víctor Tuninetti[b], Laurent Duchêne[a], Anne Marie Habraken[a,c]

[a] ArGEnCo Department, MSM team, University of Liège, Quartier POLYTECH 1, 9 allée de la Découverte, 4000 Liège, Belgium

[b] Department of Mechanical Engineering, Universidad de La Frontera, Francisco Salazar 01145, Temuco 4780000, Chile

[c] Fonds de la Recherche Scientifique –F.R.S.–F.N.R.S. Belgium, 5 rue d'Egmont 1000 Bruxelles, Belgium

*   Corresponding author: ce.rojasulloa@uliege.be


Keywords

Abstract

This work provides a numerical framework for the accurate prediction of operational life of metallic components exhibiting a non-classical creep behavior under constant loadings and very high temperature. A modified Graham-Walles type analytical viscoplastic function is implemented into a Chaboche unified viscoplastic constitutive model. The numerical model is integrated into the finite element software Lagamine following a fully-implicit two-step radial return mapping algorithm. The non-linear system of equations is solved using a robust Newton-Raphson method. The computational efficiency of the model is enhanced by implementing a sub-step routine, thereby decreasing the average number of iterations of the finite element software. The validation of the model is performed using experimental data available in the literature on the non-classical creep behavior of Incoloy 800H, a Ni-superalloy exhibiting a two-step creep strain rate minima attributed to multiple complex dislocation-precipitate interactions.

1. Introduction

Creep is the presence of an evolving permanent deformation experienced by materials under constant load at high temperature (usually above 0.5 times the melting point temperature)[1]. Creep mechanical response is different for any given material as it relies on its microstructural features. For many metallic materials, one can identify 3 creep stages: a 1st stage, where the creep mechanism (i.e., vacancy diffusion or dislocation) is initiated; a 2nd stage, where the interaction between creep mechanisms with grain boundaries and precipitates result in a steady-state creep rate; and a final 3rd stage, where the effect of damage accumulation leads to the loss of load carrying capacity of the material. This type of behavior is hereafter referred to as "classical". The three classical creep stages are presented in **Fig. 1a**.

Accurate operational life prediction of critical metallic components undergoing high thermal loadings is today a subject of significant research and scientific interest [2,3]. Standard methods consisting in the analytical prediction of a chosen failure criterion (e.g., time-to 1% strain, buckling, time-to-tertiary creep, etc.) as function of material loadings (e.g., stress, temperature) are still popular [4]. However, the reliability of data extrapolation is limited to certain stress-temperature ranges, and factors such as material microstructural features and environmental conditions are often not addressed [5,6]. Modern engineering developments concerning high-efficient technologies entail materials withstanding very-high temperatures and/or complex thermal cycles, where creep-fatigue interaction, non-classical creep responses and environmental effects must be taken into account [7–10]. Such is the case of Incoloy 800H, a Ni-superalloy developed during the 1950s with the aim of combining a good creep and corrosion resistance while achieving high cost efficiency [11]. Within temperatures beyond 760℃ and stresses roughly below 50 [MPa], the creep behavior of this alloy is reported to exhibit a one or two-step creep strain rate minima. Experimental studies on 800H [12–14] and similar austenitic Ni-Cr alloys [15,16] attribute the first minimum creep strain rate (mcr_1 in **Fig. 1b**) to the pinning of dislocations produced by the precipitation of MC carbides. The subsequent creep strain rate increment is produced by the dissolution of these precipitates, inducing a dynamic recovery effect as dislocations are unpinned. The second minimum (mcr_2) is only observed during long-term high-temperature creep tests at very-low stresses [12]. Based on macroscopic observations, the authors from [12] attributed this response to a nitridation-induced creep strain hardening produced by the precipitation of intragranular Cr and Al nitrides. Based on interrupted creep tests and metallurgic characterization, more recent studies conducted on similar austenitic Ni-Cr alloys exhibiting a similar creep response [15,16] attribute the mcr_2 to a grain boundary

precipitate strengthening (GBPS) phenomenon induced by massive intragranular precipitation of $M_{23}C_6$ carbides. This non-classical two-step minimum creep behavior alongside the possible creep micromechanical features involved in each stage are illustrated in **Fig. 1b**.
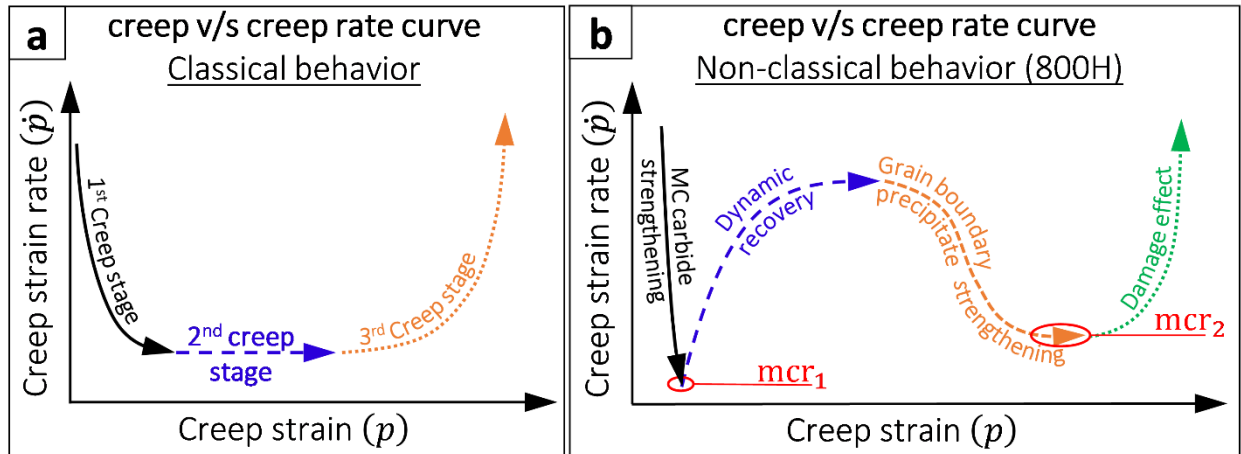
Fig. 1: Graphical illustration of: (**a**) classical creep – creep strain rate curves with 3 creep stages, and (**b**) non-classical creep strain – creep strain rate curves exhibited by Incoloy 800H for low mechanical stress and high temperature loadings.

The mechanical behavior of materials undergoing complex thermomechanical loadings is often studied via numerical simulations using the finite element (FE) method. In this context, the suitability of the constitutive law is key to achieve accurate predictions. Unified viscoplastic constitutive models (UVCMs) are preferred as they provide a numerically efficient and physically accurate representation of the plastic and viscous deformations as part of a single inelastic phenomenon[17,18]. Chaboche-type UVCMs are highlighted in this field due to their high adaptability and accuracy in the prediction of creep-fatigue life of metallic components [19]. Conventional material models of this family describe ratcheting (plastic strain accumulation within cyclic loadings) and creep-fatigue interactions using complex backstress formulations [20]. In these laws, viscoplastic deformations are modeled using a single viscosity function [19]. Both backstress and viscosity functions are in essence intended to describe the creep hardening of the material until the steady state creep rate is reached (i.e., classical 1st and 2nd creep stages, see **Fig. 1a**) [19]. In addition, a continuum damage mechanics (CDM) approach enables the integrated computation and prediction of loss of load carrying capacity of the material (3rd creep stage). This is performed by considering a unitary damage variable D ($0 \leq D < D_{FRAC}$) evolving as creep and creep-fatigue viscoplastic deformations increase. The material is considered fractured when a damage threshold D_{FRAC} is reached. A well-identified model of such a kind provides a good approximation of the remaining operational life of the component [21].

A conventional Chaboche UVCM was firstly applied to predict the creep response of 800H in air at 980°C and 14 [MPa] initial stress, where a two-step creep strain rate minima is observed [22]. This numerical model is based on the work of R. Ahmed et al. [23–25], and was implemented in FE software Lagamine by H. Morch [26] following a semi-coupled damage approach and a fully implicit integration scheme. Inelastic deformations are modeled via a single Norton viscosity function. The creep damage accumulation is predicted using a Kachanov creep damage model [27]. Material parameters were extracted from available datasheets [28,29] as well as literature on the subject [30]. Constitutive law parameters (Norton viscosity function and damage) were identified using an in-house developed Python-based optimization software [31]. The model parameters as well as the viscoplastic and damage equations for the model are provided in **Appendix A**. The true creep strain calculated using this conventional UVCM is presented in blue in **Fig. 2**. The results evidence that conventional single-hardening power-law viscoplastic formulations are unsuitable for non-classical creep behavior (see **Fig. 1b**). The predicted creep strain does not develop into the continuous creep hardening and softening phenomena observed beyond the stagnation of the Norton viscoplastic law. Moreover, the negligible effect of creep damage accumulation (red curve in **Fig. 2**) on the predicted true creep strain curve highlights the need for a new viscosity function and/or CDM formulation.
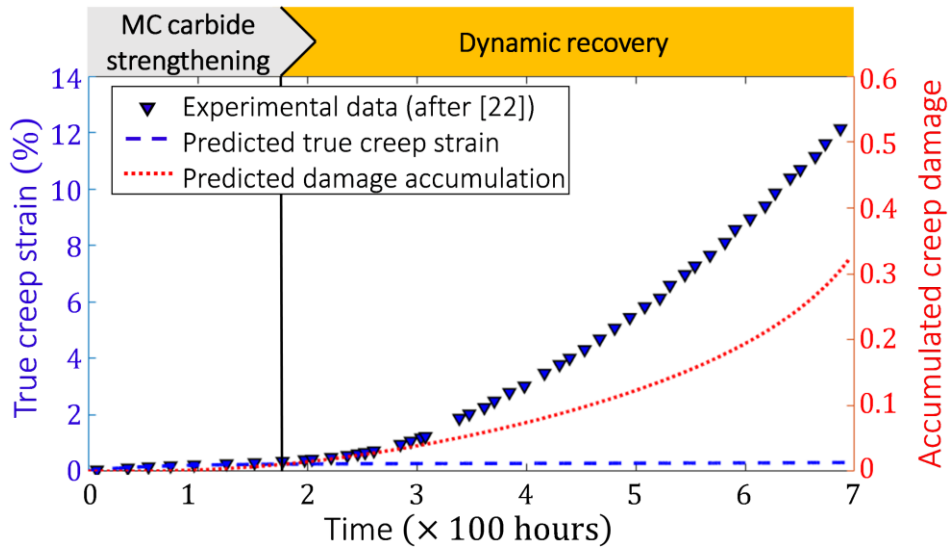
Fig. 2: True creep strain and damage accumulation predicted by a conventional Chaboche UVCM applied to non-classical creep behavior of 800H alloy.

With the objective of modeling the complex creep behavior of **Fig. 1b**, a modified Graham-Walles (mGW) type viscosity function is chosen. Initially developed as an analytical creep model [32], the Graham-Walles approach is formulated as a summation of non-linear functions, where the creep rate of the material is calculated as a function depending on the creep strain, temperature, and effective stress. Each function represents a different viscous phenomenon such as creep hardening or softening. The summation of these functions depicts a viscous behavior ruled by different creep mechanisms and/or creep stages at various moments. In addition, the chosen mGW-type CDM approach addressing creep and creep-fatigue interaction damage evolution is implemented. Both viscous and damage mGW-type functions used in Section 2 were originally developed in TU Darmstadt in cooperation with Aachen University. Operating together, these scientists have demonstrated the high reliability and accuracy of the viscosity function in the prediction of operational life of alloy 602 components subjected to low and high frequency cyclic thermal loadings [21,33–36].

The mathematical formulation of the UVCM presented in Section 2 emphasizes the proposed mGW viscoplastic features addressing complex viscoplastic behavior, creep-fatigue interaction, and coupled damage evolution. The fully-implicit FE implementation of the model is explained in detail in Section 3. Results of the application of the viscoplastic model for creep strain and creep life prediction of 800H alloy within non-classical creep regimes are presented in Section 4. Computational efficiency and overall numerical convergence of the model are also ascertained within. Finally, conclusions and future prospects on the research are summarized in Section 5.

All the numerical results presented hereafter deal with uniaxial cases. However, tensorial implementation was performed and checked by multiple multiaxial FE simulations not reproduced here for shortness [26].

2. UVCM formulation

The numerical modeling of the mechanical behavior of materials defines a scalar yield surface function Φ representing the current state of the material within the stress space. Mechanical loadings found within the elastic domain will give Φ values smaller than 0, whereas those found within the viscoplastic domain will result in the evolution of the yield surface towards $\Phi=0$. The function describing the yield surface of the UVCM is the von Mises yield criterion. The von Mises equivalent stress is calculated by solving the J_2-type function given in (1), where the material yielding is linked to the second stress tensor invariants.

$$J_2(\widetilde{\boldsymbol{\sigma}} - \mathbf{X}) = \left[\frac{3}{2}(\widetilde{\mathbf{S}} - \mathbf{X}):(\widetilde{\mathbf{S}} - \mathbf{X})\right]^{\frac{1}{2}} \tag{1}$$

In (1), $\widetilde{\boldsymbol{\sigma}}$ is the effective stress tensor, $\widetilde{\mathbf{S}}$ is the deviatoric form of the effective stress tensor, and $\mathbf{X}$ is the backstress tensor. Following the hypothesis of strain equivalency [37], the relationship between the Cauchy stress tensor $\boldsymbol{\sigma}$ and its effective counterpart is given by $\widetilde{\boldsymbol{\sigma}} = (1 - D)^{-1}\boldsymbol{\sigma}$, where D is a state variable indicating the local unitary damage ($0 \leq D < 1$). This CDM approach is chosen because of its reliability and accurate physical representation of the loss of load carrying capacity of the material it provides.

The deviatoric-effective stress tensor is calculated by:

$$\widetilde{\mathbf{S}} = \widetilde{\boldsymbol{\sigma}} - \frac{1}{3}tr(\widetilde{\boldsymbol{\sigma}})\mathbf{I} \tag{2}$$

where $\mathbf{I}$ is the 2nd order identity tensor.

The function Φ defining the yield criterion is presented in (3),

$$\Phi = J_2(\widetilde{\boldsymbol{\sigma}} - \mathbf{X}) - \sigma_y \leq 0 \tag{3}$$

where σ_y is the current yield stress of the material. The evolution of σ_y is ruled by the Voce isotropic hardening law. The formulation of which is given by $\sigma_y = \sigma_0 + R(p)$, where σ_0 is the initial yield stress of the material, and $R(p)$ is the hardening function, expressed in its variational form in (4),

$$\dot{R} = -\mathrm{B}(Q - R)\dot{p} \tag{4}$$

where Q is the hardening saturation value, B is the hardening saturation rate, and $\dot{p}$ is the equivalent inelastic strain rate.

Following the Chaboche-type UVCM formulation [19], the total backstress tensor $\mathbf{X}$ is calculated as the sum of the contribution of multiple Armstrong-Frederick (AF)-type backstress equations $\mathbf{X}_i$, where $i=1,nAF$. The general form of the singular backstress tensorial equation in its variational form is provided hereafter:

$$\dot{\mathbf{X}} = \sum_{i=1}^{nAF}\left[\frac{2}{3}C_i\dot{\boldsymbol{\epsilon}}^p - \gamma_i(\dot{\mathbf{X}}_i - \dot{\mathbf{Y}}_i)\dot{p} - \mathrm{b}_iJ_2(\mathbf{X}_i)^{(\mathrm{r}_i-1)}\mathbf{X}_i + \frac{1}{C_i}(\partial_T C_i)\dot{T}\mathbf{X}_i\right] \tag{5}$$

where $\dot{\mathbf{Y}}_i$ is a static-recovery function, $\dot{\mathbf{X}}_i$ is the ith contribution to the AF backstress tensor, $\dot{\boldsymbol{\epsilon}}^p$ is the inelastic strain rate tensor, T is the temperature, $\dot{T}$ is the temperature rate, and C_i, γ_i, b_i and r_i are material parameters.

Each term *i* in (5) models a plastic event related to a different mechanism (short- or long-term hardening, for instance due to microstructure evolution). This allows for modeling complex mechanical responses present within cyclic thermomechanical loadings [23,24,38]. For each term *i*, phenomena such as dynamic recovery [39], static recovery [40,41], and non-isothermal plasticity [42] are addressed within different parts of the equation. Following the developments of Yaguchi et al. [43,44], rectification of the mean stress of the material as consequence of static-recovery effects is introduced within the static recovery term $\dot{\mathbf{Y}}$. Based on this approach, accurate predictions of the number of cycles before rupture have been reported for Ni [25,38,45] and steels [46,47] alloys. Furthermore, a strain-memory surface function [40,48] within the parameter γ_i entailed to the second dynamic recovery term in (5) is introduced in order to accurately predict unconventional ratcheting regimes (i.e., non-Masing behavior) observed in austenitic alloys [24,25,49] undergoing non-proportional stress and strain controlled cyclic loadings. Although not addressed within our case study (creep strain prediction at constant thermomechanical loadings), all these features are included for the sake of possible future applications enhancing the capabilities of the constitutive law. Detailed mathematical description and application of the features described hereabove can be found in the works of Ahmed et al. [24,25] and Morch et al. [38].

In order to enable the UVCM to predict non-classical viscoplastic deformations, a mGW-type viscosity function is used. The evolution of the equivalent inelastic strain rate $\dot{p}$ is modeled as a summation of terms explicitly dependent on $\tilde{\boldsymbol{\sigma}}$, $\mathbf{X}$, p, D and T, whereas the time t remains an implicit variable. The mGW-type viscosity function is presented in its rate form in (6):

$$\dot{p} = \sum_{j=1}^{nVP}\left[\mathrm{K}_j \exp\left(\frac{T}{\mathrm{C}_{\mathrm{q}_j}}\right)J_2(\tilde{\boldsymbol{\sigma}} - \mathbf{X})^{\mathrm{n}_j}p^{\mathrm{m}_j}\right] + \mathrm{K}_{\mathrm{T}}|\dot{T}|J_2(\tilde{\boldsymbol{\sigma}} - \mathbf{X})p^{\mathrm{m}_{\mathrm{T}}} \tag{6}$$

where K_j, n_j, m_j, $\mathrm{C}_{\mathrm{q}j}$, K_{T} and m_{T} are material constants to be identified. Inelastic deformations related to static thermal loadings (i.e., $\dot{T} = 0$) are entailed to the summation of terms j=1:nVP, whereas those related to the presence of temperature gradients (i.e., $\dot{T} \neq 0$) are computed with the last term (subindex T). The total equivalent inelastic strain is calculated as the summation of nVP+1 independent functions, each one associated with a different hardening or softening phenomenon. The adaptability of this formulation for the prediction of a non-classical creep behavior is represented in **Fig. 3**, where a total of 3 functions are analytically fitted onto an experimental $\dot{p} - p$ creep curve exhibited by Incoloy 800H at 1000°C and an initial stress of 35 [MPa].
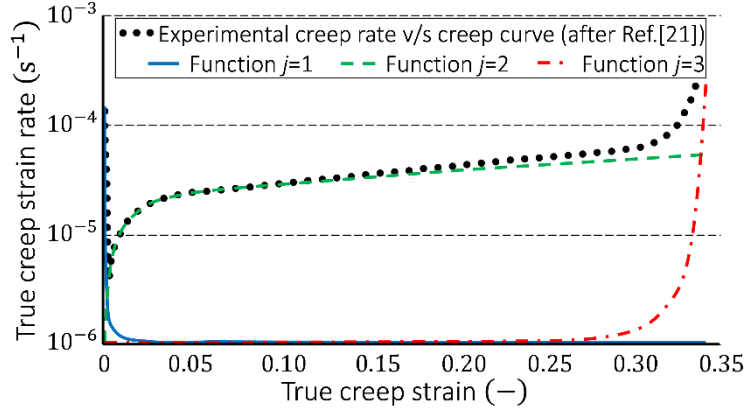
Fig. 3: Analytical fit of experimental non-classical Incoloy 800H creep curve at 1000°C and 35 [MPa] using 3 mGW viscosity functions *j*.

The implemented coupled damage formulation follows a mGW-type formulation approach, where the total damage increment is calculated as the sum of two phenomenological functions representing the creep and the creep-fatigue contributions. This damage formulation, developed in Darmstadt TU, has reported successful results for prediction of damage accumulation in Ni-alloy 602 [21,33,35]. The function is presented in its rate form in (7):

$$\dot{D} = K_D J(\tilde{\sigma} - X) + K_{TD}|\dot{T}|p^{m_{TD}} \tag{7}$$

where K_D, K_{TD} and m_{TD} are material parameters. In (7), the first term with subindex D is entitled to the creep damage equation, whereas the second term intended for computation of creep-fatigue interaction damage contribution is identified by subindex TD.

2.1. Parametric dependency to temperature

Materials submitted to high thermal loads often exhibit reversible and permanent changes in their mechanical properties due to the evolution of their microstructure [14,50,51]. Changes of the reversible type are phenomenologically addressed within this UVCM by introducing parametric dependency to the temperature on certain user-defined material parameters. A total of 5 approaches are implemented and left as a user-choice within the software: constant (no explicit temperature dependency), single exponential equation (8), double exponential equation (9), 3rd-degree polynomial (10) and Logarithmic (11) equations. Studies conducted on Hastelloy A230 by Morch et al.[38] show that inter- and extrapolated data obtained using single and double exponential approaches provide high reliability, numerical efficiency and robustness. The use of single exponential equations was preferred due to their high adaptability in [52], whereas double

exponential dependency proved more suitable for describing the parametric evolution of hardening material parameters [38]. The parametric equations are described in detail in **Table 1**.

Table 1: Summary of functions defining the parametric dependency to temperature of material parameters implemented within the UVCM. A_i are user-defined constants.
*: absolute temperature (K).

Type of equation	Equation	
Single Arrhenius equation [52]	$P(T) = A_1 \left[1 - A_2 \exp\left(\dfrac{T}{A_3}\right) \right]$	(8)
Double Arrhenius equation [38]	$P(T) = A_1 \left\{ \left[1 - A_2 \exp\left(\dfrac{T}{A_3}\right) \right] + \left[1 - A_4 \exp\left(\dfrac{T}{A_5}\right) \right] \right\}$	(9)
3-degree polynomial [30]	$P(T) = A_1 [1 + A_2(T - A_5) + A_3(T - A_5)^2 + A_4(T - A_5)^3]$	(10)
Logarithmic*	$P(T) = A_1 \left[1 + A_2 \ln\left(\dfrac{T}{A_3}\right) \right]$	(11)

As observed experimentally in other Ni-alloys [25,53], the maximum temperature reached during thermo-mechanical fatigue (TMF) loadings entails permanent changes in the material microstructure. Following the pioneering developments of [53,54], Ahmed et al.[24] introduced permanent changes in material parameters as function of the maximum temperature in the thermal history (T^{max}). The parameters affected are mainly the elastic modulus E and the parameter controlling the rate of evolution of the strain memory surface (see [24,40,48]). Detailed physical and mathematical background of these approaches can be found in [24,53,54].

3. Integration algorithm

The constitutive law presented hereabove was implemented in the FE software Lagamine, a ULiège FE code developed since the 1980s [55]. A two-level algorithm operating at each integration point of the FE mesh is executed for each time step to compute the local state variables of the material. Let us consider the current $(n+1)^{th}$ time step designated as t_{n+1}, where the actual time increment is given by $\Delta t_{n+1} = t_{n+1} - t_n$. The global level aims to compute the nodal forces and kinematic variables. This is performed by executing a main Newton-Raphson algorithm formed from a 1-level Taylor expansion of the equation describing the discrete equilibrium condition. Convergence in this main level is achieved when the out-of-balance forces and out-of-balance kinematic variables are found below the user-defined maximum admissible error. In case convergence is not reached after a

maximum of user-defined global iterations, the time increment for the step is reduced. This occurs consecutively until either convergence or a minimum time increment is reached. If no convergence is achieved after a minimum time increment is reached, the algorithm stops.

The local level of this algorithm operates within the constitutive law integration of the material. It aims to compute the local material compliance matrix and stress tensor in the current (n+1) configuration ($\mathbb{C}_{n+1}$ and $\boldsymbol{\sigma}_{n+1}$), which are function of the local state variables of the material. For calculating these last ones, the local state variables of the material in the reference (nth) configuration and the current global level guess of DOF values at the current time increment Δt_{n+1} (i.e., temperature increment ΔT_{n+1} and the strain increment $\Delta\boldsymbol{\epsilon}_{n+1}$) are taken into consideration. Extending the work of Ahmed et al.[23,24] and Morch et al.[38] towards a fully coupled damage formulation of an UVCM, the integration algorithm described hereafter consists in the execution of the elastic predictor and coupled viscoplastic-damage corrector method: a two-step algorithm. The 1st step (elastic predictor), explained in detail in Section 3.1, works on the hypothesis of a fully elastic material. If the elastic behavior is verified, all state variables are updated accordingly. Otherwise, the material behavior is confirmed as viscoplastic. In such case, the 2nd step (viscoplastic-damage corrector) of the algorithm must be executed. Henceforth referred to as viscoplastic-damage loop, this second step is described in Section 3.2.

3.1. Elastic trial

Neglecting any inelastic strain or damage increments, the elastic contribution of the strain tensor in the step (i.e., elastic predictor) is calculated by subtracting the thermal strain tensor from the total strain tensor, i.e.: $\Delta\boldsymbol{\epsilon}_{n+1}^{e} = \Delta\boldsymbol{\epsilon}_{n+1} - \Delta\boldsymbol{\epsilon}_{n+1}^{th}$. A trial stress in the current configuration is later computed as $\boldsymbol{\sigma}_{n+1}^{TRIAL} = \boldsymbol{\sigma}_n + \Delta\boldsymbol{\sigma}_{n+1}^{TRIAL}$. The stress variation in the step is calculated using the Hooke's law while acknowledging thermal effects:

$$\Delta\boldsymbol{\sigma}_{n+1}^{TRIAL} = \Delta\mathbb{C}_{n+1}^{e}\boldsymbol{\epsilon}_{n+1}^{e} + \mathbb{C}_{n+1}^{e}\Delta\boldsymbol{\epsilon}_{n+1}^{e} = \left(\frac{d\mathbb{C}^{e}}{dT}\Delta T\right)_{n+1}\boldsymbol{\epsilon}_{n+1}^{e} + \mathbb{C}_{n+1}^{e}\Delta\boldsymbol{\epsilon}_{n+1}^{e} \tag{12}$$

where $\mathbb{C}^{e}$ is the elastic compliance matrix.

Based on the trial stress tensor, a trial backstress $\mathbf{X}_{n+1}^{TRIAL}$ under the premise of possible non-zero backstress components and possible temperature gradients affecting the static recovery and its temperature rate terms is also calculated. Neglecting any effects of inelastic strain and damage increment, the discretization of the ith extended A-F kinematic hardening equation on the time-step is:

$$\frac{\mathbf{X}_{i_{n+1}}^{TRIAL} - \mathbf{X}_{i_n}}{\Delta t_{n+1}} = -b_i J_2\big(\mathbf{X}_{i_{n+1}}^{TRIAL}\big)^{(r_i-1)} \mathbf{X}_{i_{n+1}}^{TRIAL} + \frac{1}{C_i}(\partial_T C_i)_{n+1} \dot{T}_{n+1} \mathbf{X}_{i_{n+1}}^{TRIAL} \tag{13}$$

In order to solve (13) for $\mathbf{X}_{i_{n+1}}^{TRIAL}$, acknowledging its non-linearity, a brief local Newton-Raphson (NR) algorithm is implemented. For this purpose, the trial backstress tensor $\big(\mathbf{X}_{i_{n+1}}^{TRIAL}\big)$ is expressed as a function of its reference state counterpart $\big(\mathbf{X}_{i_n}\big)$:

$$\mathbf{X}_{i_{n+1}}^{TRIAL} = \left[\frac{1}{1 + b_i \Delta t_{n+1} J_2(\mathbf{X}_{i_{n+1}}^{TRIAL})^{(r_i-1)} - \frac{1}{C_i}(\partial_T C_i)_{n+1}\Delta T_{n+1}} \right] \mathbf{X}_{i_n} = \omega_{i_{n+1}} \mathbf{X}_{i_n} \tag{14}$$

The local NR algorithm is formulated by calculating the J_2 modules of (14), from which a local residual function $\mathcal{F}_{g_i} = J_2\big(\mathbf{X}_{i_{n+1}}^{TRIAL}\big) - J_2\big(\mathbf{X}_{i_n}\big)\omega_{i_{n+1}} = 0$ is formed. The final form of the local NR algorithm in the $(k+1)^{th}$ iteration is given in Eq.(15). The algorithm iterates until a user-defined maximum admissible error $\xi_{\mathcal{F}}$ is reached (i.e., $\mathcal{F}_{g_i} \leq \xi_{\mathcal{F}}$).

$$J_2\big(\mathbf{X}_{i_{n+1}}^{TRIAL}\big)_{k+1} = J_2\big(\mathbf{X}_{i_{n+1}}\big)_k - \left. \frac{\mathcal{F}_{g_i}}{\partial_{J_2(\mathbf{x}_{i_{n+1}})}\mathcal{F}_{g_i}} \right|_k \tag{15}$$

The purely-elastic behavior hypothesis is then verified by computing the yield function (3) using the trial stress and backstress tensors. The hypothesis is confirmed if the magnitude of the yield function is found to be lower or equal to zero, i.e., $f_y \leq 0$. In such case, all the state variables of the material are updated consequently: stress tensor $\boldsymbol{\sigma}_{n+1} = \boldsymbol{\sigma}_{n+1}^{TRIAL}$, backstress tensor $\mathbf{X}_{n+1} = \sum \mathbf{X}_{i_{n+1}}^{TRIAL}$, total strain tensor $\boldsymbol{\epsilon}_{n+1} = \boldsymbol{\epsilon}_n + \Delta \boldsymbol{\epsilon}_{n+1}^e$, equivalent inelastic strain $p_{n+1} = p_n$ and damage $D_{n+1} = D_n$.

Otherwise (i.e., $\Phi > 0$), the material mechanical response is found within a viscoplastic-damage regime; the elastic hypothesis is discarded, and a viscoplastic-damage loop must be executed in order to calculate the state variables.

3.2. Viscoplastic-damage loop

In this second step, an iterative elastic predictor – plastic corrector method known as the radial return mapping algorithm is executed. The algorithm iterates on the basis of the plastic flow rule [56,57]. The normal vector defining the plastic flow direction is given by (16).

$$\mathbf{n}^{\mathrm{x}} = \partial_{\tilde{\mathrm{S}}} J_2(\widetilde{\boldsymbol{\sigma}} - \mathbf{X}) = \frac{3}{2} \frac{\tilde{\mathbf{S}} - \mathbf{X}}{J_2(\widetilde{\boldsymbol{\sigma}} - \mathbf{X})} \tag{16}$$

The effective normal vector is defined as $\mathbf{n} = (1 - D)^{-1}\mathbf{n}^{\mathrm{x}}$. The flow rule can thus be expressed in terms of both normal $\mathbf{n}^{\mathrm{x}}$ and effective normal $\mathbf{n}$ vectors as seen in (17).

$$\Delta\boldsymbol{\epsilon}^p = \Delta p \mathbf{n} = (1 - D)^{-1}\Delta p \mathbf{n}^{\mathrm{x}} \tag{17}$$

The unknown variables of the material in the incremental configuration (n+1) are grouped into a vector $\Delta \boldsymbol{\mathcal{W}}$:

$$\Delta \boldsymbol{\mathcal{W}} = [\Delta\boldsymbol{\epsilon}^e \quad \Delta p \quad \Delta\boldsymbol{\sigma} \quad \Delta\mathbf{X}_i \quad \Delta D]^{\mathrm{T}} \tag{18}$$

The discretized functions describing the evolution of the variables within the vector $\Delta \boldsymbol{\mathcal{W}}$ are summarized in **Table 2**.

Table 2: Summary of unknown variable increments within the viscoplastic-damage loop and equations defining their evolution.

Unknown increment	Equations	
$\Delta\boldsymbol{\epsilon}^e(\Delta p, \boldsymbol{\sigma}, \mathbf{X}, D)$	$\Delta\boldsymbol{\epsilon}^e = \Delta\boldsymbol{\epsilon} - \Delta\boldsymbol{\epsilon}^{th} - \Delta p \mathbf{n}$	(19)
$\Delta p(p, \boldsymbol{\sigma}, \mathbf{X}, D)$	$\Delta p = \left\{ \sum_{j=1}^{nVP} \left[\mathrm{K}_j \exp\left(\frac{T}{\mathrm{C}_{\mathrm{q}_j}}\right) J_2(\widetilde{\boldsymbol{\sigma}} - \mathbf{X})^{\mathrm{n}_j} p^{\mathrm{m}_j} \right] + \mathrm{K}_\mathrm{T}|\dot{T}| J_2(\widetilde{\boldsymbol{\sigma}} - \mathbf{X}) p^{\mathrm{m}_\mathrm{T}} \right\} \Delta t$	(20)
$\Delta\boldsymbol{\sigma}(\Delta\boldsymbol{\epsilon}^e, D)$	$\Delta\widetilde{\boldsymbol{\sigma}} = \mathbb{C}^e \Delta\boldsymbol{\epsilon}^e$	(21)
$\Delta\mathbf{X}_i(\Delta p, \boldsymbol{\sigma}, \mathbf{X}, D)$	$\Delta\mathbf{X}_i = \frac{2}{3}\mathrm{C}_i\Delta p \mathbf{n} - \gamma_i(\mathbf{X}_i - \mathbf{Y}_i)\Delta p - \mathrm{b}_i J_2(\mathbf{X}_i)^{(\mathrm{r}_i - 1)}\mathbf{X}_i\Delta t + \frac{1}{\mathrm{C}_i}(\partial_T \mathrm{C}_i)\Delta T \mathbf{X}_i$	(22)
$\Delta D(p, \boldsymbol{\sigma}, \mathbf{X}, D)$	$\Delta D = \mathrm{K}_\mathrm{D} J_2(\widetilde{\boldsymbol{\sigma}} - \mathbf{X})\Delta t + \mathrm{K}_\mathrm{TD}|\Delta T| p^{\mathrm{m}_\mathrm{TD}}$	(23)

The non-linearity of the system and the strong dependence between the functions presented in **Table 2** evidence the need for an adequate numerical method capable of reaching a solution while preserving computational efficiency. Within this framework, a thorough study on the speed, robustness and computational efficiency of different order NR approaches was conducted by Morch et al.[58]. It was concluded that the classic 1-step NR method provides the highest average speed and robustness, and is therefore used in this work.

A local residual vector $\mathbf{R}_{loc}(\Delta \mathcal{W})$ is formed based on the functions defining the evolution of the unknown variables:

$$\mathbf{R}_{loc}(\Delta \mathcal{W}) = \begin{Bmatrix} \Delta \boldsymbol{\epsilon}^e + \Delta \boldsymbol{\epsilon}^{th} - \Delta \boldsymbol{\epsilon} + \Delta p \mathbf{n} \\ \Delta p - \left\{ \sum_{j=1}^{nVP} \left[\mathrm{K}_j \exp\left(\frac{T}{\mathrm{C}_{\mathrm{T}j}}\right) J_2(\widetilde{\boldsymbol{\sigma}} - \mathbf{X})^{\mathrm{n}_j} p^{\mathrm{m}_j} \right] + \mathrm{K}_{\mathrm{T}} |\dot{T}| J_2(\widetilde{\boldsymbol{\sigma}} - \mathbf{X}) p^{\mathrm{m}_{\mathrm{T}}} \right\} \Delta t \\ \Delta \boldsymbol{\epsilon}^e - inv(\mathbb{C}^e)\widetilde{\boldsymbol{\sigma}} \\ \Delta \mathbf{X}_i - \frac{2}{3} \mathrm{C}_i \Delta p \mathbf{n} + \gamma_i (\mathbf{X}_i - \mathbf{Y}_i) \Delta p + \mathrm{b}_i J_2(\mathbf{X}_i)^{(\mathrm{r}_i - 1)} \mathbf{X}_i \Delta t - \frac{1}{C_i} (\partial_T C_i) \Delta T \mathbf{X}_i \\ \Delta D - \mathrm{K}_{\mathrm{D}} J_2(\widetilde{\boldsymbol{\sigma}} - \mathbf{X}) \Delta t - \mathrm{K}_{\mathrm{TD}} |\Delta T| p^{\mathrm{m}_{\mathrm{TD}}} \end{Bmatrix} \tag{24}$$

The final form of the NR algorithm is:

$$\Delta \mathcal{W}_{n+1}^{k+1} = \Delta \mathcal{W}_{n+1}^k - inv\big(\mathcal{J}[\mathbf{R}_{loc}(\Delta \mathcal{W})]_{n+1}^k\big)\mathbf{R}_{loc}(\Delta \mathcal{W})_{n+1}^k \tag{25}$$

where $\mathcal{J}[\mathbf{R}_{loc}(\Delta \mathcal{W})]_{n+1}^k$ is the Jacobian matrix of the local residuals vector with respect to the vector of variables (18). The form of the Jacobian matrix in conjunction with all partial derivatives concerning the algorithm are shown in detail in **Appendix A**.

The initial guess of this radial return mapping algorithm $\Delta \mathcal{W}_{n+1}^1$ contains the variables describing the overestimated yield surface $\Phi > 0$ calculated within the previous elastic trial. As such, initial guess for stress and backstress increments are defined as $\Delta \boldsymbol{\sigma}_{n+1}^{TRIAL}$ and $\Delta \mathbf{X}_{i_{n+1}}^{TRIAL}$ respectively. However, given the direct mathematical relationship exhibited by the equations describing the evolution of p (20) and D (23), different initial guess variables are introduced for $\Delta \boldsymbol{\epsilon}_{n+1}^e$, Δp_{n+1} and ΔD_{n+1} according to the material behavior exhibited in the previous step. In case no inelastic deformations are detected within the previous step, $\Delta \boldsymbol{\epsilon}_{n+1}^e$ is considered equivalent to the total mechanical strain, whereas a small initial value of 10^{-3} is introduced in Δp and ΔD in order to impose possible inelastic

deformations and damage accumulation. Otherwise, $\Delta \boldsymbol{\epsilon}^e_{n+1} = \mathbf{0}_{6\times 6}$, $\Delta p = \Delta p_n$ and $\Delta D = \Delta D_n$. These conditions are expressed in (26).

$$\Delta \boldsymbol{\mathcal{W}}^1_{n+1} = \begin{cases} \left[(\Delta \boldsymbol{\epsilon} - \Delta \boldsymbol{\epsilon}^{th})_{n+1} \quad ; \quad 10^{-3} \quad ; \quad \Delta \boldsymbol{\sigma}^{TRIAL}_{n+1} \quad ; \quad \Delta \mathbf{X}^{TRIAL}_{i_{n+1}} \quad ; \quad 10^{-3} \right]^{\mathrm{T}} \quad if \; \Delta p_n = 0 \\ \left[\mathbf{0}_{6\times 6} \quad ; \quad \Delta p_n \quad ; \quad \Delta \boldsymbol{\sigma}^{TRIAL}_{n+1} \quad ; \quad \Delta \mathbf{X}^{TRIAL}_{i_{n+1}} \quad ; \quad \Delta D_n \right]^{\mathrm{T}} \qquad\qquad otherwise \end{cases} \qquad (26)$$

In order to preserve computational efficiency, the calculation of the inverse of the Jacobian matrix from (25) is avoided. Instead, a new linear system formed on the basis of (25) by $inv\big(\mathcal{J}[\mathbf{R}_{loc}(\Delta \boldsymbol{\mathcal{W}})]^k_{n+1}\big)\mathbf{R}_{loc}(\Delta \boldsymbol{\mathcal{W}})^k_{n+1} = \mathbf{A}^{k+1}_{n+1}$ is solved at each NR iteration by means of an LU-decomposition. This approach has demonstrated to increase the overall computational efficiency of the subroutine while maintaining high accuracy and robustness. This new local system of equations is:

$$\mathbf{R}_{loc}(\Delta \boldsymbol{\mathcal{W}})^k_{n+1} = -\mathcal{J}[\mathbf{R}_{loc}(\Delta \boldsymbol{\mathcal{W}})]^k_{n+1}\mathbf{A}^k_{n+1} \qquad (27)$$

Convergence for the $(k+1)$th NR iteration is achieved when the norm of the magnitude of the local residual vector $\left[\mathbf{R}_{loc}(\Delta \boldsymbol{\mathcal{W}})^{k+1}_{n+1} : \mathbf{R}_{loc}(\Delta \boldsymbol{\mathcal{W}})^{k+1}_{n+1}\right]^{0.5}$ is lower or equal than the maximum admissible error of $\xi_{\mathrm{R}_{loc}}$ defined by the user. In such case, the variables in the $(n+1)$th iteration are updated on the basis of the incremental values calculated as $\Delta \boldsymbol{\mathcal{W}}^{k+1}_{n+1}$.

Divergence within this NR algorithm is confirmed if the norm of local residual vector is larger than the maximum admissible error after a maximum of user-defined $k_{\max}$ NR iterations is reached, or if values with no physical meaning appear within the variables (e.g., $\Delta p < 0$ or $\Delta \dot{p} < 0$). In case of divergence, the default algorithm (consisting in the reduction of the global time-step Δt_{n+1} and recalculation of the initial guess DOF) is firstly avoided by means of the activation of a local sub-step algorithm working within the constitutive law level. The current guess of the DOF kinematic variable vector is consequently subdivided by the total number of sub-steps (Nss) introduced by the user, and it linearly increases based on the sub-step counter u. This approach is intended to preserve computational efficiency during large complex simulations, where a global decrement of the time increment on the step would result in larger computational times. The condition expressed in (26) extends to this sub-step algorithm, and is executed at the beginning of each sub-step accordingly. A

brief flowchart summarizing the constitutive law integration scheme performed at each time step is presented in **Fig. 4**.
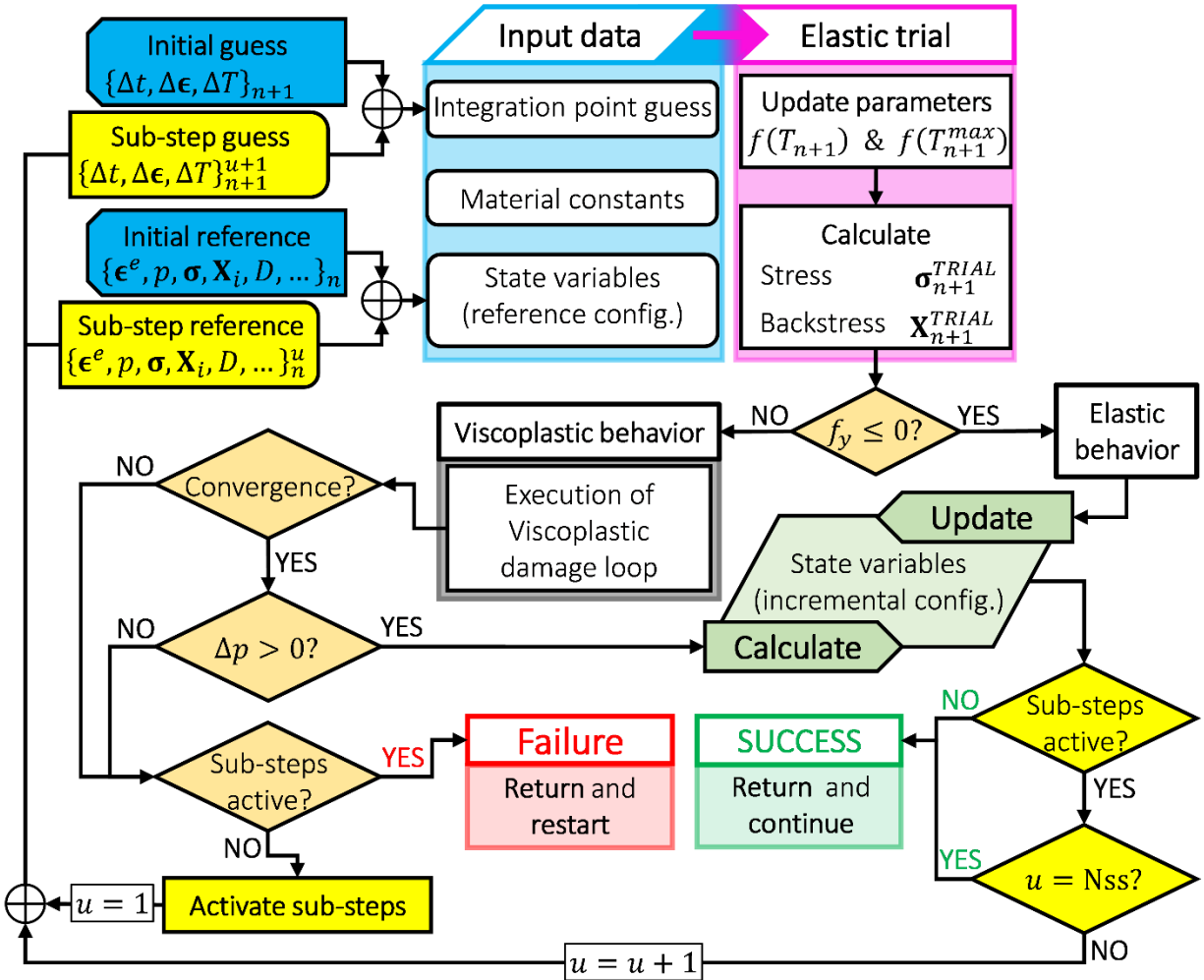
Fig. 4: Flowchart describing the integration algorithm of the constitutive law.

4. Results and discussion

In this section, results obtained from FE simulations executed using the UVCM implemented into Lagamine FE software are presented and analyzed. Section 4.1 addresses the validation of the viscosity function chosen to predict the non-classical viscous behavior of Incoloy 800H. The numerical convergence and computational efficiency of the model is later ascertained in Section 4.2.

4.1. Case study validation

The choice made for this modified Chaboche-type UVCM is hereafter checked within the context of our case study: an accurate prediction of non-classical viscoplastic behavior of 800H alloy under very high thermal and low mechanical loadings. Given the focus of this study, constitutive law features related to cyclic thermomechanical loadings (such as kinematic hardening, mean stress evolution, strain memory surface, creep-fatigue interaction, and thermal gradient dependent features) will not be taken into consideration. In addition, calculation of isotropic hardening is omitted due to its reported negligible effect in similar Austenitic Ni-Cr alloys as viscous deformations occur during static loadings and below the yielding point of the material [23,24].

A total of four experimental true creep strain rate (s^{-1}) v/s true creep strain curves extracted from available scientific literature are addressed for the purpose of this study: two curves from uniaxial creep (constant axial load) tests conducted by (Guttmann & Bürgel, 1983)[12] and two curves from uniaxial relaxation (constant axial stress) tests conducted by (K. Tachibana et al., 1998)[59]. A detailed summary of the experimental dataset used for this study is given in Table 3.

Table 3: Key features of tests used for identification and validation of the modified Chaboche-type UVCM.

Test description	Tag	Temperature	Stress	Reference
Uniaxial creep tests	GB-1	1000 °C	11 [MPa]	[12]
(Guttmann & Bürgel, 1983)	GB-2	1000 °C	35 [MPa]	[12]
Uniaxial relaxation tests	KT-1	950°C	45 [MPa]	[59]
(K. Tachibana et al., 1998)	KT-2	900°C	35 [MPa]	[59]

Currently the calculation of the coupled damage accumulation is left out of the scope of this study due to the lack of data on the subject provided within the available experimental data summarized in Table 3. Consequently, only material parameters and mGW viscosity function for inelastic strains prediction at constant temperature (i.e., subindex j in (6)) are considered.

Material parameters are introduced within the constitutive law following the parametric temperature dependency approach summarized in **Table 1**. More specifically, the elastic modulus (E) and Poisson's ratio (v) are introduced as 3rd degree polynomials (10). A summary of the parameters and their correspondent standard deviation is provided in [30].

Optimal parameters for each mGW-type viscosity function are found following a direct analytical identification procedure seeking to minimize the standard deviation calculated between experimental and analytical curves. Following the "1 equation per phenomenon" logic previously expressed in **Fig. 3**, the total number nVP of mGW equations (i.e., equations j=1, nVP in (6)) is determined by the number of viscous phenomena existing within the experimental curves.

Initial diffusional-driven and dislocation-driven viscous deformations are observed across all experimental curves. This is directly followed by a tertiary creep stage in experimental datasets GB-1, KT-1, and KT-2, thus leaving the total number of mGW equations in nVP=3 for these datasets. In the case of GB-1, the tertiary creep stage is preceded by a nitridation-induced hardening phenomenon, thus leaving the total number of mGW equations in nVP=4.

Even though both literature sources deal with the same material, the undisclosed microstructural uncertainties inherent as both come from different batches can greatly affect the further viscous behavior of the alloy.[22] Given the fact that such uncertainties fall out of the scope of this study, and in order to better assess numerical capabilities of the UVCM, each experimental source (GB and KT) is dealt with as coming from different materials. Two analytical identification procedures are performed separately per literature source, and two different sets of parameters are consequently identified.

The composition of each mGW-type viscosity function as the sum of nVP equations f is described in Table 4, where each alphabetic sub-index indicates a different equation and phenomenon.

Table 4: Description of mGW viscous function used per each dataset curve

Viscous function	Equations (j=1,nVP)				Summation in formula
Dataset curve	1	2	3	4	j=1,nVP
GB-1	f_A	f_B	f_C	f_D	$\dot{p} = f_A + f_B + f_C + f_D$
GB-2	f_A	f_B	f_E		$\dot{p} = f_A + f_B + f_E$
KT-1 and KT-2	f_F	f_G	f_H		$\dot{p} = f_F + f_G + f_H$

As seen in Table 4, a total of 3 sets of parameters (2 possibilities for GB data set and 1 single data set for Tachibana case) and 8 different equations were identified. A summary of the analytically identified parameters for all 8 equations is presented in Table 5.

Table 5: mGW viscosity law equation parameters identified analytically for describing the non-classical viscous behavior of Incoloy 800H undergoing very high-temperature and low-stress creep and relaxation tests.

| Equation	Phenomenon	K	C_q	m	n
f_A	Diffusional-driven	$2.00E-20$	-20.88	5.01	-10.20
f_B	Dislocation-driven	$1.00E-19$	50.00	3.71	0.60
f_C	Nitridation + tertiary creep	$-2.80E-14$	50.00	0.02	2.48
f_D		$1.00E-02$	50.00	0.03	9.80
f_E	Tertiary creep	$1.00E-02$	50.00	2.00	29.55
f_F	Diffusional-driven	$1.02E-30$	-116.00	0.20	-1.33
f_G	Dislocation-driven	$1.73E-33$	15.04	0.20	0.32
f_H	Tertiary creep	$1.00E-17$	15.04	0.20	36.00

Given the nearly uniaxial stress state exhibited by smooth bar samples used during the literature experiments, the material is modeled into the FE software Lagamine [55] as a single tridimensional element of the type BWD3T [60,61]. This hexahedral element type considers 8 nodes, 4 DOF per node (orthogonal spatial coordinates and temperature) and a single point of integration. A sketch describing the boundary conditions imposed in this simplified material model is presented in **Fig. 5**.
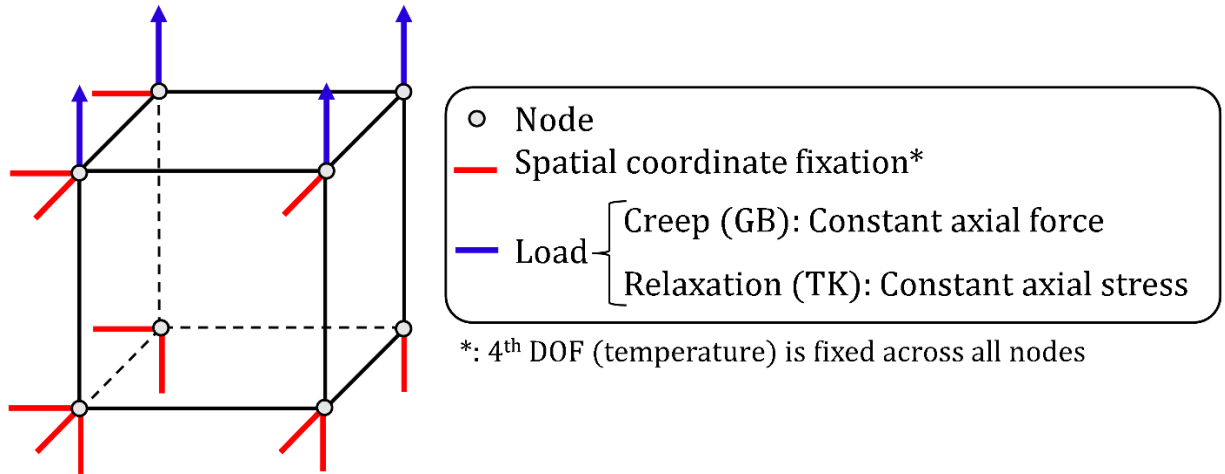
Fig. 5: Description of simplified single-element FE model of the type BWD3T used for all numerical simulations.

The loadings and boundary conditions applied to the simplified FE model presented in **Fig. 5** replicate the addressed experimental creep and relaxation tests. FE simulations are executed in Lagamine, using the implemented Chaboche-type constitutive law and the parameters presented hereabove in Table 5. An initial time step of approximately 0.01% of the time-to-rupture (t_r) of the alloy under the specific experimental conditions of the simulation is imposed. In case of convergence, this time step increases until a maximum time increment of 0.1% of the same t_r and held constant until the simulation end. Newton-Raphson iterations at the viscoplastic-damage loop of the constitutive law (see flowchart in **Fig. 4**) are limited to a maximum number of 400 iterations. A maximum local residual magnitude of 1×10^{-5} is imposed as a convergence criterion for the calculation of the trial backstress ($\xi_{\mathcal{F}}$) and variables within an inelastic regime ($\xi_{R_{loc}}$). The sub-step routine is set as inactive for these simulations.

The predicted t_r and true creep strain versus true creep strain rate curves are extracted and compared with the available experimental curves in **Fig. 6** along with their respective standard deviations (St.Dev.).
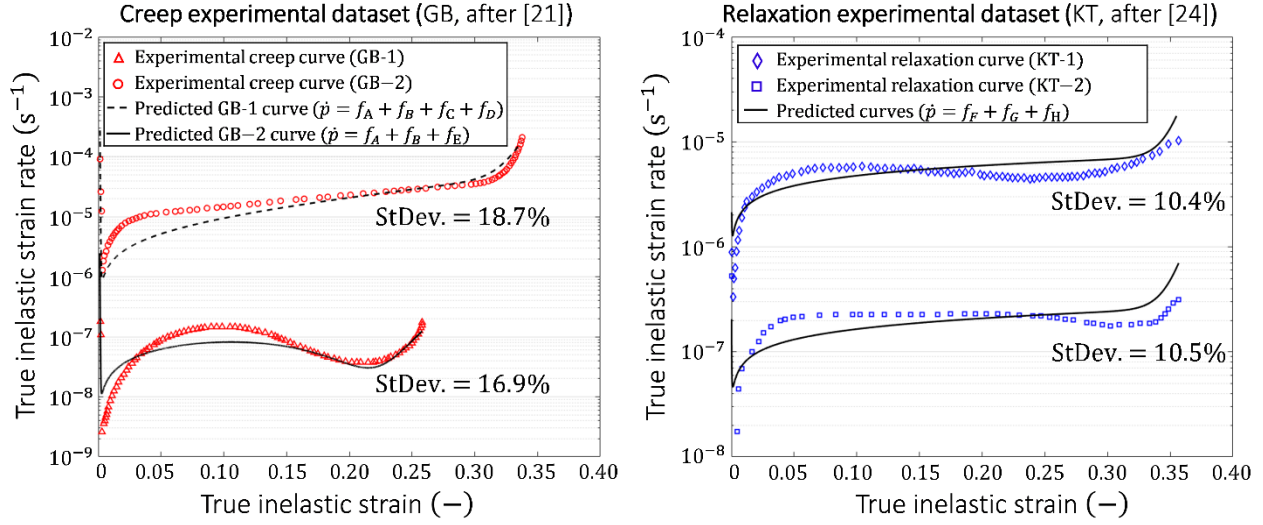
Fig. 6: Comparison of predicted and experimental $\dot{p}$-p curves of Incoloy 800H exhibiting non-classical creep and relaxation viscoplastic regimes.

As seen in **Fig. 6**, the experimental non-classical creep and relaxation inelastic regimes exhibited by 800H alloy are predicted by the UVCM with admissible accuracy. The standard deviation calculated for the GB experimental dataset curves is almost 80% higher than the one calculated for the TK experimental dataset. This is attributed to the steep difference between the dislocation-driven inelastic regimes exhibited by these two curves, entailing a higher error than during the direct analytical viscosity function fit.

Numerical predictions of the time-to-1% inelastic strain ($t_{1\%}$) and t_r are compared with their respective experimental counterparts in Table 6 to further assess the capabilities of the UVCM. In particular, $t_{1\%}$ is chosen as it is often used as a failure criterion in industrial applications.

Table 6: Prediction of time-to-1% inelastic strain and time-to-rupture using the proposed UVCM.

Dataset curve	time-to-1% inelastic strain (h)		time-to-rupture (h)	
	Experimental	Numerical	Experimental	Numerical
GB-1	384	144.1 ± 27	1480	1450 ± 271
GB-2	1.7	2.1 ± 0.4	8	9.5 ± 1.6
TK-1	2.3	1.9 ± 0.2	25.9	20.0 ± 2.0
TK-2	60	47.5 ± 5.0	654.1	567.1 ± 60

In general, the results presented in Table 6 verify that the prediction of the global non-classical inelastic behavior of the case-study alloy is successful. Numerical predictions of t_r are found well within admissible accuracy margins, averaging a percentile error of $-4.8^{+9.7\%}_{-7.6\%}$. In contrast, $t_{1\%}$ predictions present a higher average percentile error of $-19.3^{+3.7\%}_{-9.7\%}$. The larger error calculated for this last case can be attributed to the local loss of inelastic behavior prediction accuracy that takes place as the material behavior becomes transitional.

4.2. Assessment of numerical convergence

Loss of numerical convergence due to maximum number of iterations reached was detected in the early stages of FE simulations intended to replicate experimental tests belonging to datasets GB-1, GB-2, and TK-1 (see **Fig. 6**). This took place only within the steep inelastic strain rate slope change $(\partial_p \dot{p})$, occurring within mcr_1 (see **Fig. 1b**). In absence of an active sub-step algorithm, this divergence led to a global time step decrement and high computational times.

The effect of the proposed sub-step algorithm on the computational performance of the UVCM has been studied. FE simulations address the three experimental datasets exhibiting divergence. No change in the initial and maximum time increments for the time step or the Newton-Raphson algorithm convergence criteria ($\xi_{\mathcal{F}}$ and $\xi_{R_{loc}}$) compared to Section 4.1 is applied. The sub-step algorithm is activated, and the effect of a wide range of number of sub-steps (Nss) ranging from 1 to 5000 imposed across the three simulations is computed. The numerical performance is assessed in terms of the normalized maximum number of iterations executed within the global FE algorithm level, whereas the computational efficiency is assessed in terms of the normalized CPU time spent until the simulation is completed. Results are presented in **Fig. 7**.

21
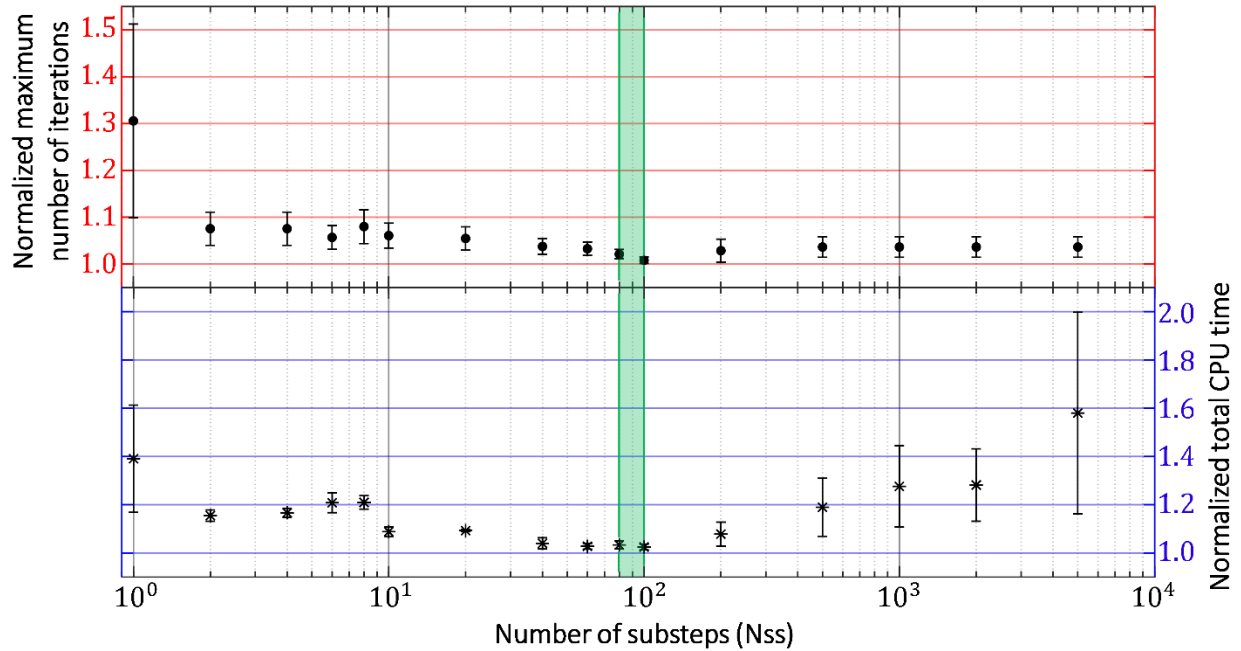
Fig. 7: Numerical and computational performance of the UVCM applied on non-classical viscous behavior of Incoloy 800H with a wide range of number of sub-steps (Nss). The green zone highlights the optimal Nss where the lowest number of iterations and lowest CPU time is achieved.

The results show that the implementation of a sub-step algorithm with a Nss ranging between 80 and 100 (highlighted with green in **Fig. 7**) can greatly decrease the computational times and the total number of iterations within the global level of the FE algorithm. Compared to the by-default inactive sub-step performance of the software, improvements in computational and numerical performance are also observed within values of Nss found anywhere below this optimal range (i.e., 2<Nss≤100). In contrast, increasing the Nss beyond such range shows highly detrimental effects as CPU times tend to increase consistently.

5. Conclusions

In this work, a mGW-type viscosity function was implemented into a Chaboche-type constitutive model following a unified viscoplastic formulation. The UVCM was successfully implemented in Lagamine following a fully implicit two-step elastic predictor and viscoplastic-damage corrector method. A sub-step algorithm was included to further improve the computational and numerical performance of the model. Numerical simulations were performed in the context of the case study,

seeking to replicate the reportedly non-classical viscoplastic regimes exhibited by Incoloy 800H under very-high thermal and low-mechanical loadings. Experimental correlation of the numerical creep and relaxation curves obtained demonstrate that such creep and relaxation material behavior can be predicted with good accuracy.

The implemented sub-step algorithm with the integration scheme of the constitutive law managed to decrease the computational times and overall number of Newton-Raphson iterations taking place within the global FE algorithm level. It improves computational efficiency up to 38% and numerical convergence up to a 33%.

The proposed UVCM exhibits remarkable capabilities for predicting complex non-classical viscoplastic regimes where continuous hardening and softening behaviors are observed. The work presented herein proposes a re-definition of the viscosity function as a methodology to enhance the prediction capabilities of Chaboche models. In conjunction with other well-studied modifications (such as new backstress formulations, damage, and equivalent effective stress formulations), this new tool gives means to explore new frontiers in engineering and material sciences.

The ability of each mGW function to be correlated to a specific creep micromechanics phenomenon enables the identification of parameters to be performed via direct identification procedure. The creep curves database needed for a reliable identification of parameters is foreseen to be obtained via physical experimental tests and the simulation results of virtual tests. The latter could be achieved for instance via the development and application of a mean-field model that takes into consideration all microstructural features known to be involved in the viscoplastic response of the alloy [62].

Acknowledgements

Conflict of interest

The authors declare no conflict of interest.

Appendix A. Parameters and equations involved in the obtention of Fig.2

In this section, a brief insight on the conventional Chaboche UVCM used for the obtention of **Fig. 2** alongside with the parameters used during the FE simulation are provided. As discussed earlier, the constitutive law developed and implemented by H. Morch [26] integrates a Norton-type viscosity function and a semi-coupled CDM formulation. The viscosity function is presented in its continuum form (A.1), where K is the drag stress and N is the viscous exponent.

$$\dot{p} = \langle \frac{J_2(\widetilde{\boldsymbol{\sigma}} - \mathbf{X}) - \sigma_y}{K} \rangle^{\text{N}} \tag{A.1}$$

Damage evolution is predicted using the Rabotnov-Kachanov creep CDM approach. The damage function is presented in its continuum form in (A.2), where S_c, S_{ce} and K_c are parameters to be identified.

$$\dot{D}_c = \left[\frac{J_2(\widetilde{\boldsymbol{\sigma}} - \mathbf{X})}{S_c} \right]^{S_{ce}} \frac{1}{(1 - D)^{k_c}} \tag{A.2}$$

The parameters used to obtain the creep strain and damage evolution curves presented in **Fig. 2** are provided in Table A.1. Material parameters were extracted from [28–30], whereas those related to the Norton viscosity function (K,N) and creep damage function (S_c, S_{ce}, K_c) were found throughout an inverse identification procedure (Levenberg-Marquardt algorithm, see [31]). The objective of the optimization algorithm was to minimize the error function comparing the experimental creep curve of 800H obtained at 980°C and 14.7 [MPa] extracted from [22] with the model prediction. In order to maximize chances of success, the curves were only addressed up until the start of the second precipitate strengthening process (see orange curve in **Fig. 1b**). Due to the very low stress and strain, the creep damage parameters evidenced negligible effect on the resulting creep response.

Table A.1: Summary of parameters used during the first FE simulation using a conventional Chaboche constitutive law.

	Parameter	Symbol	Magnitude	Source
Material parameters	Elastic modulus	E	7.30 [GPa]	[30]
	Poisson's ratio	v	0.31	[30]
	Thermal dilatation coefficient	α	0.0182×10^{-6} K^{-1}	[28,29]
	Yield stress	σ_0	10.50 [MPa]	[30]
Isotropic hardening parameters (4)	Saturation rate	b	0	*Optimized*
	Saturation value	Q	5×10^{-4}[MPa]	*Optimized*
Viscosity function parameters(A.1)	Drag stress	K	5×10^{8} [MPa]	*Optimized*
	Exponent	N	1.20	*Optimized*
Rabotnov-Kachanov's **creep damage** parameters (A.2)	Creep damage parameter	S_c	1×10^{3}	*Optimized*
	Creep damage parameter	S_{ce}	1.50	*Optimized*
	Creep damage parameter	k_c	2.00	*Optimized*

Appendix B. Components of local residuals Jacobian matrix

The Jacobian matrix resulting from the application of the viscoplastic loop NR algorithm is presented in (B.1).

$$\mathcal{J}\{\mathbf{R}_{loc}\} = \begin{Bmatrix} \partial_{\Delta\boldsymbol{\epsilon}^e}R_{\boldsymbol{\epsilon}^e} & \partial_{\Delta p}R_{\boldsymbol{\epsilon}^e} & \partial_{\Delta\boldsymbol{\sigma}}R_{\boldsymbol{\epsilon}^e} & \partial_{\Delta\mathbf{x}_i}R_{\boldsymbol{\epsilon}^e} & \partial_{\Delta D}R_{\boldsymbol{\epsilon}^e} \\ \partial_{\Delta\boldsymbol{\epsilon}^e}R_p & \partial_{\Delta p}R_p & \partial_{\Delta\boldsymbol{\sigma}}R_p & \partial_{\Delta\mathbf{x}_i}R_p & \partial_{\Delta D}R_p \\ \partial_{\Delta\boldsymbol{\epsilon}^e}R_{\boldsymbol{\sigma}} & \partial_{\Delta p}R_{\boldsymbol{\sigma}} & \partial_{\Delta\boldsymbol{\sigma}}R_{\boldsymbol{\sigma}} & \partial_{\Delta\mathbf{x}_i}R_{\boldsymbol{\sigma}} & \partial_{\Delta D}R_{\boldsymbol{\sigma}} \\ \partial_{\Delta\boldsymbol{\epsilon}^e}R_{\mathbf{X}_i} & \partial_{\Delta p}R_{\mathbf{X}_i} & \partial_{\Delta\boldsymbol{\sigma}}R_{\mathbf{X}_i} & \partial_{\Delta\mathbf{x}_i}R_{\mathbf{X}_i} & \partial_{\Delta D}R_{\mathbf{X}_i} \\ \partial_{\Delta\boldsymbol{\epsilon}^e}R_D & \partial_{\Delta p}R_D & \partial_{\Delta\boldsymbol{\sigma}}R_D & \partial_{\Delta\mathbf{x}_i}R_D & \partial_{\Delta D}R_D \end{Bmatrix} \quad \text{(B.1)}$$

The partial derivatives expressed in (B.1)

are henceforth defined row-by-row. The partial derivatives of the local residual function intended to calculate the elastic strain tensor are shown in (B.2)-(B.6).

$$\partial_{\Delta \boldsymbol{\epsilon}^e} R_{\boldsymbol{\epsilon}^e} = \mathbf{I}_4 \tag{B.2}$$

$$\partial_{\Delta p} R_{\boldsymbol{\epsilon}^e} = \mathbf{n} \tag{B.3}$$

$$\partial_{\Delta \boldsymbol{\sigma}} R_{\boldsymbol{\epsilon}^e} = \frac{\Delta p}{(1 - D)} \partial_{\Delta \boldsymbol{\sigma}} \mathbf{n}^{\mathrm{x}} \tag{B.4}$$

$$\partial_{\Delta \mathbf{x}_i} R_{\boldsymbol{\epsilon}^e} = \frac{\Delta p}{(1 - D)} \partial_{\Delta \mathbf{x}_i} \mathbf{n}^{\mathrm{x}} \tag{B.5}$$

$$\partial_{\Delta D} R_{\boldsymbol{\epsilon}^e} = \frac{\Delta p}{(1 - D)} \partial_{\Delta D} \mathbf{n}^{\mathrm{x}} \tag{B.6}$$

The partial derivatives of the local residual function intended to calculate the incremental inelastic strain from the mGW-type viscosity function are presented in (B.7) -(B.11) .

$$\partial_{\Delta \boldsymbol{\epsilon}^e} R_p = [0\ 0\ 0\ 0\ 0\ 0] \tag{B.7}$$

$$\partial_{\Delta p} R_p = 1 - \sum_{j=1}^{nVP} \left[K_j \exp\left(\frac{T}{C_{q_j}}\right) J_2(\tilde{\boldsymbol{\sigma}} - \mathbf{X})^{n_j} m_j p^{(m_j - 1)} \Delta t \right] - K_T |\Delta T| J_2(\tilde{\boldsymbol{\sigma}} - \mathbf{X}) m_T p^{(m_T - 1)} \tag{B.8}$$

$$\partial_{\Delta \boldsymbol{\sigma}} R_p = - \left\{ \sum_{j=1}^{nVP} \left[K_j \exp\left(\frac{T}{C_{q_j}}\right) n_j J_2(\tilde{\boldsymbol{\sigma}} - \mathbf{X})^{(n_j - 1)} p^{m_j} \Delta t \right] + K_T |\Delta T| p^{m_T} \right\} \partial_{\Delta \boldsymbol{\sigma}} J_2(\tilde{\boldsymbol{\sigma}} - \mathbf{X}) \tag{B.9}$$

$$\partial_{\Delta \mathbf{x}_i} R_p = - \left\{ \sum_{j=1}^{nVP} \left[K_j \exp\left(\frac{T}{C_{q_j}}\right) n_j J_2(\tilde{\boldsymbol{\sigma}} - \mathbf{X})^{(n_j - 1)} p^{m_j} \Delta t \right] + K_T |\Delta T| p^{m_T} \right\} \partial_{\Delta \mathbf{x}_i} J_2(\tilde{\boldsymbol{\sigma}} - \mathbf{X}) \tag{B.10}$$

$$\partial_{\Delta D} R_p = - \left\{ \sum_{j=1}^{nVP} \left[K_j \exp\left(\frac{T}{C_{q_j}}\right) n_j J_2(\tilde{\boldsymbol{\sigma}} - \mathbf{X})^{(n_j - 1)} p^{m_j} \Delta t \right] + K_T |\Delta T| p^{m_T} \right\} \partial_{\Delta D} J_2(\tilde{\boldsymbol{\sigma}} - \mathbf{X}) \tag{B.11}$$

The partial derivatives of the local residual function for the calculation of the stress tensor are given in

$$\partial_{\Delta \boldsymbol{\epsilon}^e} R_{\boldsymbol{\sigma}} = \mathbf{I}_4 \tag{B.12}$$

$$\partial_{\Delta p} R_{\boldsymbol{\sigma}} = [0\ 0\ 0\ 0\ 0\ 0]^{\mathrm{T}} \tag{B.13}$$

$$\partial_{\Delta \boldsymbol{\sigma}} R_{\boldsymbol{\sigma}} = -\frac{1}{(1-D)} inv(\mathbb{C}^e) \tag{B.14}$$

$$\partial_{\Delta \mathbf{X}_i} R_{\boldsymbol{\sigma}} = \mathbf{0}_{6\times 6} \tag{B.15}$$

$$\partial_{\Delta D} R_{\boldsymbol{\sigma}} = -\frac{\boldsymbol{\sigma}}{(1-D)^2} inv(\mathbb{C}^e) \tag{B.16}$$

The partial derivatives for the ith extended AF backstress tensor local residual function are given in

$$\partial_{\Delta \boldsymbol{\epsilon}^e} R_{\mathbf{X}_i} = \mathbf{0}_{6\times 6} \tag{B.17}$$

$$\partial_{\Delta p} R_{\mathbf{X}_i} = -\frac{2}{3} C_i \mathbf{n} + \gamma_i (\mathbf{X}_i - \mathbf{Y}_i) \tag{B.18}$$

$$\partial_{\Delta \boldsymbol{\sigma}} R_{\mathbf{X}_i} = -\frac{2}{3} C_i \frac{\Delta p}{(1-D)} \partial_{\Delta \boldsymbol{\sigma}} \mathbf{n}^{\mathrm{x}} \tag{B.19}$$

$$\partial_{\Delta \mathbf{X}_i} R_{\mathbf{X}_i} = \left[1 + \gamma_i \Delta p + \mathrm{b}_i \Delta t J_2(\underline{\mathbf{X}}_i)^{(\mathrm{r}_i - 1)} - \frac{1}{C_i}(\partial_T C_i)\Delta T\right] \mathbf{I}_4 + \frac{2}{3} C_i \frac{\Delta p}{(1-D)} \partial_{\mathbf{S}} \mathbf{n}^{\mathrm{x}} -$$
$$\gamma_i \Delta p \partial_{\Delta \mathbf{X}_i} \mathbf{Y}_i + \frac{3}{2} \mathrm{b}_i \Delta t (\mathrm{r}_i - 1) J_2(\underline{\mathbf{X}}_i)^{(\mathrm{r}_i - 3)} \mathbf{X}_i \otimes \mathbf{I}_4 \otimes \mathbf{X}_i \tag{B.20}$$

$$\partial_{\Delta D} R_{\mathbf{X}_i} = -\frac{2}{3}\frac{C_i \Delta p}{(1-D)} \partial_{\Delta D} \mathbf{n}^{\mathrm{x}} \tag{B.21}$$

Partial derivatives of the local residual function intended for the calculation of the coupled damage accumulation are provided in (B.22) (B.26)

$$\partial_{\Delta\boldsymbol{\epsilon}^e} R_D = [0\ 0\ 0\ 0\ 0\ 0] \tag{B.22}$$

$$\partial_{\Delta p} R_D = -K_{TD}|\Delta T| m_{TD} p^{(m_{TD}-1)} \tag{B.23}$$

$$\partial_{\Delta\boldsymbol{\sigma}} R_D = -K_D \Delta t \, \partial_{\Delta\boldsymbol{\sigma}} J_2(\widetilde{\boldsymbol{\sigma}} - \mathbf{X}) \tag{B.24}$$

$$\partial_{\Delta\mathbf{X}_i} R_D = -K_D \Delta t \, \partial_{\Delta\mathbf{X}_i} J_2(\widetilde{\boldsymbol{\sigma}} - \mathbf{X}) \tag{B.25}$$

$$\partial_{\Delta D} R_D = 1 - K_D \Delta t \, \partial_{\Delta D} J_2(\widetilde{\boldsymbol{\sigma}} - \mathbf{X}) \tag{B.26}$$

Some important partial derivatives appearing in equations presented hereabove, entailed to the normal vector $\mathbf{n}^x$ or the equivalent von Mises effective stress $J_2(\widetilde{\boldsymbol{\sigma}} - \mathbf{X})$ are presented in (B.27) (B.32)

$$\partial_{\Delta\boldsymbol{\sigma}} \mathbf{n}^x = \frac{1}{(1-D)J_2(\widetilde{\boldsymbol{\sigma}} - \mathbf{X})} \left[\frac{3}{2} \mathbf{I}_4 - \mathbf{n}^x \otimes \mathbf{n}^x \right] \otimes \left[\mathbf{I}_2 - \frac{1}{3} \mathbf{I}_1 \otimes \mathbf{I}_1 \right] \tag{B.27}$$

$$\partial_{\Delta\mathbf{X}_i} \mathbf{n}^x = -\partial_{\Delta\tilde{s}} \mathbf{n}^x \tag{B.28}$$

$$\partial_{\Delta s} \mathbf{n}^x = \frac{1}{(1-D)J_2(\widetilde{\boldsymbol{\sigma}} - \mathbf{X})} \left[\frac{3}{2} \mathbf{I}_4 - \mathbf{n}^x \otimes \mathbf{n}^x \right] \tag{B.29}$$

$$\partial_{\Delta D} \mathbf{n}^x = \frac{1}{(1-D)^2 J_2(\widetilde{\boldsymbol{\sigma}} - \mathbf{X})} \left[\frac{3}{2} \mathbf{I}_4 - \mathbf{n}^x \otimes \mathbf{n}^x \right] \otimes \mathbf{S} \tag{B.30}$$

$$\partial_{\Delta\boldsymbol{\sigma}} J_2(\widetilde{\boldsymbol{\sigma}} - \mathbf{X}) = \mathbf{n} \otimes \left[\mathbf{I}_2 - \frac{1}{3} \mathbf{I}_1 \otimes \mathbf{I}_1 \right] \tag{B.31}$$

$$\partial_{\Delta D} J_2(\widetilde{\boldsymbol{\sigma}} - \mathbf{X}) = \mathbf{n}^x \odot \mathbf{S} \tag{B.32}$$

In case of law convergence, the consistent tangent operator of the local system $\mathbb{C} = d_{\boldsymbol{\epsilon}} \boldsymbol{\sigma}$ is calculated from the inverse of the Jacobian matrix resulting from the last successful NR iteration at the end of the step. The stress-strain relationship is obtained from the components related to (B.4). In case of sub-step routine activation, the consistent tangent operator is calculated at the end of each sub-step and accumulated into a matrix $\mathbb{C}_{Nss}$. The final $\mathbb{C}$ at the step is later calculated as the average of the $\mathbb{C}_{Nss}$ as seen in (B.33).

$$\mathbb{C} = \frac{\mathbb{C}_{Nss}}{N_{ss}} \tag{B.33}$$

References

[1] F.R.N. Nabarro, de Villiers, The Physics of creep, Taylor & Francis, 1995.

[2] D. Sun, J. Huo, S. An, Experimental and Numerical Study of Turbine Blade Fatigue Based on a Creep-Fatigue Prediction Model, Journal of Engineering Materials and Technology. 144 (2022). https://doi.org/10.1115/1.4053617.

[3] M. Sattar, A.R. Othman, S. Kamaruddin, M. Akhtar, R. Khan, Limitations on the computational analysis of creep failure models: A review, Engineering Failure Analysis. 134 (2022) 105968. https://doi.org/10.1016/j.engfailanal.2021.105968.

[4] Z. Huda, Creep Behavior of Materials, in: Mechanical Behavior of Materials, Springer International Publishing, Cham, 2022: pp. 253–265. https://doi.org/10.1007/978-3-030-84927-6_14.

[5] J. Röesler, H. Harders, M. Beaker, Mechanical Behaviour of Engineering Materials, Springer, 2007.

[6] S.R. Holdsworth, Constitutive equations for creep curves and predicting service life, in: Creep-Resistant Steels, Elsevier, 2008: pp. 403–420. https://doi.org/10.1533/9781845694012.2.403.

[7] R.W. Swindeman, D.L. Marriott, Criteria for design with structural materials in combined-cycle applications above 815°F, J. Eng. Gas Turbines Power. 116 (1993) 11. https://doi.org/10.1115/1.2906827.

[8] R.W. Swindeman, M.J. Swindeman, W. Ren, Can Coverage of Alloy 800H in ASME Section III Subsection NH be Extended to 850°C?, in: Volume 6: Materials and Fabrication, ASMEDC, Vancouver, BC, Canada, 2006: pp. 521–528. https://doi.org/10.1115/PVP2006-ICPVT-11-93333.

[9] W. Ren, R. Swindeman, A Review on Current Status of Alloys 617 and 230 for Gen IV Nuclear Reactor Internals and Heat Exchangers 1, Journal of Pressure Vessel Technology. 131 (2009) 044002. https://doi.org/10.1115/1.3121522.

[10] W. Ren, R. Swindeman, Status of Alloy 800 H in Considerations for the Gen IV Nuclear Energy Systems, Journal of Pressure Vessel Technology. 136 (2014) 054001. https://doi.org/10.1115/1.4025093.

[11] J.C.M. Farrar, The alloy tree, Woodhead Publishing Limited, Cambridge, England, 2004.

[12] V. Guttmann, R. Bürgel, Creep–structural relationship in steel alloy 800 H at 900–1000°C, Metal Science. 17 (1983) 549–555. https://doi.org/10.1179/030634583790420475.

[13] H.P. Degischer, H. Aigner, H. Lahodny, K. Spiradek, Qualification of stationary creep of the carbide precipitating alloy 800H, in: High Temperature Alloys, Springer, Dordrecht, 1987: pp. 487–498.

[14] K. Spiradek, H.P. Degischer, H. Lahodny, Correlation between microstructure and the creep behaviour at high temperature of alloy 800 H, in: Materials Science, International Atomic Energy Agency (IAEA), Vienna, Austria, 1989: pp. 54–65.

[15] T. Hatakeyama, K. Sawada, K. Sekido, T. Hara, K. Kimura, Influence of dynamic microstructural changes on the complex creep deformation behavior of 25Cr–20Ni–Nb–N steel at 873 K, Materials Science and Engineering: A. 814 (2021) 141270. https://doi.org/10.1016/j.msea.2021.141270.

[16] T. Hatakeyama, K. Sawada, K. Sekido, T. Hara, K. Kimura, Microstructural factors of the complex creep rate change in 18Cr–9Ni–3Cu–Nb–N steel, Materials Science and Engineering: A. 831 (2022) 142225. https://doi.org/10.1016/j.msea.2021.142225.

[17] G. Kang, Ratchetting: Recent progresses in phenomenon observation, constitutive modeling and application, International Journal of Fatigue. 30 (2008) 1448–1472. https://doi.org/10.1016/j.ijfatigue.2007.10.002.

[18]   T. Zhang, X. Wang, D. Zhou, R. Wang, Y. Jiang, X. Zhang, J. Gong, S. Tu, A universal constitutive model for hybrid stress-strain controlled creep-fatigue deformation, International Journal of Mechanical Sciences. 225 (2022) 107369. https://doi.org/10.1016/j.ijmecsci.2022.107369.

[19]   J.L. Chaboche, A review of some plasticity and viscoplasticity constitutive theories, International Journal of Plasticity. 24 (2008) 1642–1693. https://doi.org/10.1016/j.ijplas.2008.03.009.

[20]   N. Ohno, Recent Topics in Constitutive Modeling of Cyclic Plasticity and Viscoplasticity, Applied Mechanics Reviews. 43 (1990) 283–295. https://doi.org/10.1115/1.3119155.

[21]   N. Kaushik Karthik, Investigations on the effects of alternating temperatures on the lfetime of P-type radiant tubes, PhD thesis, RWTH Aachen University, 2020.

[22]   B. Gardiner, High temperature creep performance of alloy 800H, PhD. thesis, University of Canterbury, 2014.

[23]   R. Ahmed, P.R. Barrett, T. Hassan, Unified viscoplasticity modeling for isothermal low-cycle fatigue and fatigue-creep stress–strain responses of Haynes 230, International Journal of Solids and Structures. 88–89 (2016) 131–145. https://doi.org/10.1016/j.ijsolstr.2016.03.012.

[24]   R. Ahmed, T. Hassan, Constitutive modeling for thermo-mechanical low-cycle fatigue-creep stress–strain responses of Haynes 230, International Journal of Solids and Structures. 126–127 (2017) 122–139. https://doi.org/10.1016/j.ijsolstr.2017.07.031.

[25]   R. Ahmed, P.R. Barrett, M. Menon, T. Hassan, Thermo-mechanical low-cycle fatigue-creep of Haynes 230, International Journal of Solids and Structures. 126–127 (2017) 90–104. https://doi.org/10.1016/j.ijsolstr.2017.07.033.

[26]   H. Morch, Thermomechanical modelling of the creep-fatigue behaviour and damage of Nickel-alloy receiver tubes used in Concentrated Solar Power plants, PhD., 2022.

[27]   L. Markovich Kachanov, The theory of creep, National Leading library for Science and Technology, 1967.

[28]   Incoloy alloy 800H & 800HT, Special Metals Corporation, 2004.

[29]   NAS 800H/800T (UNS N08810/N08811), (2011).

[30]   J.P. Hammond, L.T. Ratcliff, C.R. Brinkman, M.W. Moyer, C.W. Nestor, Jr., Dynamic and Static Measurements of Elastic Constants with Data on 2 1/4 Cr-1 Mo Steel, Types 304 and 316 Stainless Steels, and Alloy 800H, Oak Ridge Laboratory, Oak Ridge, Tennessee, U.S., 1979.

[31]   E. Betaieb, L. Duchêne, A.M. Habraken, Calibration of kinematic hardening parameters on sheet metal with a Computer Numerical Control machine, International Journal of Material Forming. 15 (2022) 69. https://doi.org/10.1007/s12289-022-01714-3.

[32]   K.F. Walles, A. Graham, The relationship between the creep and tensile properties at elevated temperature of Nimonic 80-II, National gas turbine establishment, Ohio, U.S., 1953.

[33]   N. Schmitz, C. Schwotzer, H. Pfeifer, Increasing lifetime of metallic recirculating radiant tubes, Heat Processing. (2018) 8.

[34]   N.K. Karthik, N. Schmitz, H. Pfeifer, R. Schwing, S. Linn, C. Kontermann, M. Oechsner, Einfluss von Temperaturwechselbeanspruchung auf das Verformungsverhalten von Ofenkomponenten und deren Lebensdauer, Berg Huettenmaenn Monatsh. 164 (2019) 364–371. https://doi.org/10.1007/s00501-019-0882-5.

[35]   N.K. Karthik, N. Schmitz, H. Pfeifer, Effect of cyclic thermal loading on the lifetime of furnace components, in: Heat Treatment & Surface Engineering for Automotive, Associazione Italiana di Metallurgia, Bardolino, Italy, 2019: pp. 1–10.

[36]   N. Schmitz, N.K. Karthik, H. Pfeifer, J.G. Wuenning, Durability of metallic radiant tubes in galvanizing lines, in: Charleston, South Carolina, USA, 2019: p. 17.

[37]   J. Lemaitre, J.L. Chaboche, Phenomenological aspect of rupture by damage, Journal de Mécanique Appliquée. 2 (1978) 317–365.

[38]   H. Morch, L. Duchêne, R. Harzallah, V. Tuninetti, A.M. Habraken, Efficient temperature dependence of parameters for thermo-mechanical finite element modeling of alloy 230, European Journal of Mechanics - A/Solids. 85 (2021) 104116. https://doi.org/10.1016/j.euromechsol.2020.104116.

[39]   C.O. Frederick, P.J. Armstrong, A mathematical representation of the multiaxial Bauschinger effect, Mat. at High Temp. 24 (2007) 1–26. https://doi.org/10.3184/096034007X207589.

[40]   J.L. Chaboche, K.D. Van, G. Cordier, Modelization of the strain memory effect on the cyclic hardening of 316 stainless steel, in: Materials Modeling and Inelastic Analysis of Metal Structures, IASMiRT, Berlin, Germany, 1979.

[41]   J.L. Chaboche, G. Rousselier, On the Plastic and Viscoplastic Constitutive Equations—Part I: Rules Developed With Internal Variable Concept, Journal of Pressure Vessel Technology. 105 (1983) 153–158. https://doi.org/10.1115/1.3264257.

[42]   J.-D. Wang, N. Ohno, Two equivalent forms of nonlinear kinematic hardening: application to nonisothermal plasticity, International Journal of Plasticity. 7 (1991) 637–650. https://doi.org/10.1016/0749-6419(91)90048-4.

[43]   M. Yaguchi, M. Yamamoto, T. Ogata, A viscoplastic constitutive model for nickel-base superalloy, part 1: kinematic hardening rule of anisotropic dynamic recovery, International Journal of Plasticity. 18 (2002) 1083–1109. https://doi.org/10.1016/S0749-6419(01)00029-8.

[44]   M. Yaguchi, M. Yamamoto, T. Ogata, A viscoplastic constitutive model for nickel-base superalloy, part 2: modeling under anisothermal conditions, International Journal of Plasticity. 18 (2002) 1111–1131. https://doi.org/10.1016/S0749-6419(01)00030-4.

[45]   P.R. Barrett, T. Hassan, A unified constitutive model in simulating creep strains in addition to fatigue responses of Haynes 230, International Journal of Solids and Structures. 185–186 (2020) 394–409. https://doi.org/10.1016/j.ijsolstr.2019.09.001.

[46]   M. Bartošák, M. Španiel, K. Doubrava, Unified viscoplasticity modelling for a SiMo 4.06 cast iron under isothermal low-cycle fatigue-creep and thermo-mechanical fatigue loading conditions, International Journal of Fatigue. 136 (2020) 105566. https://doi.org/10.1016/j.ijfatigue.2020.105566.

[47]   M. Bartošák, Constitutive modelling for isothermal low-cycle fatigue and fatigue-creep of a martensitic steel, Mechanics of Materials. 162 (2021) 104032. https://doi.org/10.1016/j.mechmat.2021.104032.

[48]   S. Krishna, T. Hassan, I. Ben Naceur, K. Saï, G. Cailletaud, Macro versus micro-scale constitutive models in simulating proportional and nonproportional cyclic and ratcheting responses of stainless steel 304, International Journal of Plasticity. 25 (2009) 1910–1949. https://doi.org/10.1016/j.ijplas.2008.12.009.

[49]   V. Aubin, A.-L. Bulthé, S. Degallaix, P. Quaegebeur, Ratcheting behavior of a duplex stainless steel: characterization and modeling, in: Proceedings of the Ninth International Conference on the Mechanical Behavior of Materials, 2003: pp. 25–29.

[50]   L. Tan, L. Rakotojaona, T.R. Allen, R.K. Nanstad, J.T. Busby, Microstructure optimization of austenitic Alloy 800H (Fe–21Cr–32Ni)₢, Materials Science and Engineering A. (2011) 7. https://doi.org/10.1016/j.msea.2010.12.052.

[51]   H. Akhiani, M. Nezakat, M. Sanayei, J. Szpunar, The effect of thermo-mechanical processing on grain boundary character distribution in Incoloy 800H/HT, Materials Science and Engineering: A. 626 (2015) 51–60. https://doi.org/10.1016/j.msea.2014.12.046.

[52]   E. Hosseini, S.R. Holdsworth, I. Kühn, E. Mazza, Temperature dependent representation for Chaboche kinematic hardening model, Materials at High Temperatures. 32 (2015) 404–412. https://doi.org/10.1179/1878641314Y.0000000036.

[53]   B. Kleinpass, K.-H. Lang, D. Löhe, E. Macherauch, Thermal-Mechanical Fatigue Behaviour of NiCr22Co12Mo9, in: J. Bressers, L. Rémy, M. Steen, J.L. Vallés (Eds.), Fatigue under Thermal and Mechanical Loading: Mechanisms, Mechanics and Modelling: Proceedings of the Symposium Held at Petten, The Netherlands, 22–24 May 1995, Springer Netherlands, Dordrecht, 1996: pp. 327–337. https://doi.org/10.1007/978-94-015-8636-8_35.

[54]   N. Ohno, Y. Takahashi, K. Kuwabara, Constitutive Modeling of Anisothermal Cyclic Plasticity of 304 Stainless Steel, Journal of Engineering Materials and Technology. 111 (1989) 106–114. https://doi.org/10.1115/1.3226424.

[55]   University of Liège, "Lagamine FE code". http://www.lagamine.uliege.be/dokuwiki/doku.php/.

[56]   D.C. Drucker, Some implications of work hardening and ideal plasticity, Quarterly of Applied Mathematics. 7 (1950) 411–418.

[57]   J.C. Simo, T.J. Hughes, Computational inelasticity, Springer Science & Business Media, 2006.

[58]   H. Morch, S. Yuan, L. Duchêne, R. Harzallah, A.M. Habraken, A review of higher order Newton type methods and the effect of numerical damping for the solution of an advanced coupled Lemaitre damage model, Finite Elements in Analysis and Design. 209 (2022) 103801. https://doi.org/10.1016/j.finel.2022.103801.

[59]   K. Tachibana, H. Nishi, M. Eto, Y. Muto, Creep characteristics of Alloy 800H, Japan, 1998. http://inis.iaea.org/search/search.aspx?orig_q=RN:29043501.

[60]   Y.Y. Zhu, S. Cescotto, Unified and mixed formulation of the 8-node hexahedral elements by assumed strain method, Computer Methods in Applied Mechanics and Engineering. 129 (1996) 177–209. https://doi.org/10.1016/0045-7825(95)00835-7.

[61]   R.T. Jardin, V. Tuninetti, J.T. Tchuindjang, N. Hashemi, R. Carrus, A. Mertens, L. Duchêne, H.S. Tran, A.M. Habraken, Sensitivity Analysis in the Modelling of a High Speed Steel Thin-Wall Produced by Directed Energy Deposition, Metals. 10 (2020). https://doi.org/10.3390/met10111554.

[62]   F. Riedlsperger, B. Krenmayr, G. Zuderstorfer, B. Fercher, B. Niederl, J. Schmid, B. Sonderegger, Application of an advanced mean-field dislocation creep model to P91 for calculation of creep curves and time-to-rupture diagrams, Materialia. 12 (2020) 100760. https://doi.org/10.1016/j.mtla.2020.100760.